

# 3D Local Manipulation of the Metal–Insulator Transition Behavior in VO<sub>2</sub> Thin Film by Defect-Induced Lattice Engineering

Qi Jia, Jörg Grenzer, Huabing He, Wolfgang Anwand, Yanda Ji, Ye Yuan, Kai Huang, Tiangui You, Wenjie Yu, Wei Ren, Xinzhong Chen, Mengkun Liu, Stefan Facsko, Xi Wang, and Xin Ou\*

The ability to manipulate the metal–insulator transition (MIT) of metal oxides is of critical importance for fundamental investigations of electron correlations and practical implementations of power efficient tunable electrical and optical devices. Most of the existing techniques including chemical doping and epitaxial strain modification can only modify the global transition temperature, while the capability to locally manipulate MIT is still lacking for developing highly integrated functional devices. Here, lattice engineering induced by the energetic noble gas ion allowing a 3D local manipulation of the MIT in VO<sub>2</sub> films is demonstrated and a spatial resolution laterally within the micrometer scale is reached. Ion-induced open volume defects efficiently modify the lattice constants of VO<sub>2</sub> and consequently reduce the MIT temperature continuously from 341 to 275 K. According to a density functional theory calculation, the effect of lattice constant variation reduces the phase change energy barrier and therefore triggers the MIT at a much lower temperature. VO<sub>2</sub> films with multiple transitions in both in-plane and out-of-plane dimensions can be achieved by implantation through a shadow mask or multienergy implantation. Based on this method, temperature-controlled VO<sub>2</sub> metasurface structure is demonstrated by tuning only locally the MIT behavior on the VO<sub>2</sub> surfaces.

first-order MIT at a critical temperature around 341 K.<sup>[1]</sup> During the transition process, the bulk crystal structure undergoes a transformation from the insulating low-temperature monoclinic phase to the metallic high-temperature tetragonal phase.<sup>[2]</sup> The exotic MIT properties in VO<sub>2</sub> have attracted much attention due to its potential applications, including smart window,<sup>[3]</sup> transistors,<sup>[4]</sup> switching devices,<sup>[5]</sup> phase transition memory,<sup>[6]</sup> and sensors with ultrafast response.<sup>[7]</sup> However, the above practical applications were limited by the relatively high phase transition temperature of VO<sub>2</sub>. In recent years, many efforts have been carried out for the refined modification of the critical temperature to room temperature, such as chemical doping,<sup>[8]</sup> interfacial strain engineering,<sup>[9]</sup> hydrogenation,<sup>[10]</sup> ionic liquids modulation,<sup>[11]</sup> light excitation,<sup>[12]</sup> and so on. Nevertheless, these methods only permit a global tuning of the transition temperature, while the local control at micro- or even nanoscale is still chal-

lenging at this stage. The ability to nanoengineer the transition temperature, especially in a 3D space, is therefore nontrivial to realize, which is essential for the fabrication of highly integrated VO<sub>2</sub>-based novel devices and structures, such as reconfigurable electronic circuits<sup>[11a]</sup> and metamaterials.<sup>[13]</sup>

## 1. Introduction

Metal–insulator transition (MIT) is one of the most attractive phenomena in strongly correlated materials. Vanadium dioxide (VO<sub>2</sub>), a prototype correlated oxide compound, exhibits a

Q. Jia, K. Huang, Dr. T. You, Dr. W. Yu, Prof. X. Wang, Prof. X. Ou  
 State Key Laboratory of Functional Materials for Informatics  
 Shanghai Institute of Microsystem and Information Technology  
 Chinese Academy of Sciences  
 Shanghai 200050, China  
 E-mail: ouxin@mail.sim.ac.cn

Q. Jia, K. Huang, Prof. X. Wang  
 University of Chinese Academy of Sciences  
 Beijing 10049, China

Dr. J. Grenzer, Dr. Y. Ji, Y. Yuan, Dr. S. Facsko  
 Institute of Ion Beam Physics and Materials Research  
 Helmholtz-Zentrum Dresden-Rossendorf  
 Bautzner Landstrasse 400, Dresden 01328, Germany

H. He, Prof. W. Ren  
 Department of Physics  
 Shanghai University  
 99 Shangda Road, Shanghai 200444, China  
 Dr. W. Anwand  
 Institute of Radiation Physics  
 Helmholtz-Zentrum Dresden-Rossendorf  
 Bautzner Landstrasse 400, Dresden 01328, Germany

Dr. Y. Ji  
 College of Science  
 Nanjing University of Aeronautics and Astronautics  
 Nanjing 211106, China

X. Chen, Prof. M. Liu  
 Department of Physics and Astronomy  
 Stony Brook University  
 Stony Brook, NY 11794, USA

DOI: 10.1002/admi.201701268

Defect engineering has been demonstrated to be an effective approach for tailoring the physical properties in condensed-matter systems.<sup>[14]</sup> Introducing a small amount of defects into the oxide or a slight modification of the lattice constant can significantly change their physical properties.<sup>[15]</sup> Here, we demonstrate that the defect or lattice engineering by ion beam technology can be implemented to manipulate the MIT of VO<sub>2</sub> system and especially to locally change the MIT behavior of VO<sub>2</sub> thin film in the in-plane and out-of-plane dimensions. Ion beam implantation is a classic technique to manipulate the electrical properties of materials by introducing impurity dopants.<sup>[16]</sup> In such case, the modification of materials results from the electron exchange between the implanted dopant and the lattice atom. Alternatively, ion implantation enables the defect or lattice engineering in semiconductors and functional oxides, which can be applied to modify and optimize the electrical, optical, magnetic, and even mechanical properties of functional materials and devices. For instance, 2D electron gas in LaAlO<sub>3</sub>/SrTiO<sub>3</sub> can be patterned by a MeV proton beam exposure due to the effect of carrier localization.<sup>[17]</sup> Very recently, it was reported that the electrical resistivity of ferroelectric thin films was enhanced via He<sup>+</sup> implantation.<sup>[18]</sup> T. Z. Ward et al. found that the single-axis lattice of oxides can be controlled by He<sup>+</sup> implantation,<sup>[19]</sup> which shed light on the potential use of noble gas ion implantation to modify the material properties.

In this work, we show that the MIT temperature of VO<sub>2</sub> thin films can be dramatically reduced by Ne<sup>+</sup> implantation. The implantation-induced open volume defects result in a variation of the lattice parameters evidenced by the X-ray diffraction (XRD) analysis. In addition, a first-principle calculation based on density functional theory (DFT) method reveals that both the out-of-plane lattice expansion and the in-plane lattice contraction would reduce the phase change energy barrier and trigger the MIT process at a lower temperature. Furthermore, spatially separated insulator and metallic areas on VO<sub>2</sub> surfaces at room temperature were realized by area-selective ion implantation. A multilevel MIT process was observed in VO<sub>2</sub> thin film after the Ne<sup>+</sup> implantation with different energies.

## 2. Results and Discussion

VO<sub>2</sub> thin films with a thickness of about 220 nm were epitaxially grown on c-plane (0001) sapphire substrate by pulsed laser deposition (PLD). 100 keV Ne<sup>+</sup> was implanted into the as-deposited VO<sub>2</sub> thin films at room temperature. The ion fluences were  $1 \times 10^{14}$ ,  $5 \times 10^{14}$ , and  $1 \times 10^{15}$  cm<sup>-2</sup>. A virgin sample without implantation was used as a reference sample (defined as “virgin” in the following discussions). The electrical transport properties of VO<sub>2</sub> thin films were probed by the standard Van der Pauw method.<sup>[20]</sup> The temperature-dependent resistance of the virgin and Ne<sup>+</sup>-implanted VO<sub>2</sub> samples, and their corresponding differential curves were shown in Figure 1a,b, respectively. At the critical temperature around 341 K, the virgin VO<sub>2</sub> thin film exhibits a sharp phase transition from insulating state to metallic state with a four order of magnitudes change in the resistance. There is a hysteresis loop between the heating branch and cooling branch.<sup>[21]</sup> After Ne<sup>+</sup> implantation, the phase transition process occurred at a lower

temperature. And the related differential curves indicate an apparent decrease of the MIT temperature with the increasing Ne<sup>+</sup> implantation fluence. With the Ne<sup>+</sup> implantation fluence of  $1 \times 10^{14}$ ,  $5 \times 10^{14}$ , and  $1 \times 10^{15}$  cm<sup>-2</sup>, the MIT temperature of VO<sub>2</sub> thin films was reduced from 341 to 330, 297, and 275 K (black triangle symbols in Figure 1b), respectively. Figure 1c indicates an almost linear dependency of the MIT temperature of VO<sub>2</sub> samples on the Ne<sup>+</sup> fluence of  $-7.3$  K  $10^{-14}$  cm<sup>-2</sup>. In addition, an explicit broadening of the phase transition process with the increasing Ne<sup>+</sup> implantation fluence has been observed due to the inhomogeneous Ne<sup>+</sup> distribution along the out-of-plane direction.<sup>[22]</sup> Moreover, the original phase transition process (marked by the yellow dash line in Figure 1b) remains in the Ne<sup>+</sup>-implanted samples. This indicates the coexistence of the areas with different phase change temperatures in the thin film. The depth distribution profiles of Ne<sup>+</sup> ions in VO<sub>2</sub> samples were simulated by Monte Carlo simulation with the computer code of the stopping and range of ions in matter (SRIM)<sup>[23]</sup> (Figure 1d–f). For the virgin sample, there is only one homogenous area (Figure 1d) across the entire thin film so that only one phase transition process can be detected, as shown in Figure 1g. After 100 keV Ne<sup>+</sup> implantation, the concentration of Ne atoms in the films generally follows a Gaussian distribution. As shown in Figure 1e, area 1 contains a small fraction of implanted Ne<sup>+</sup> ions; therefore, it has similar properties as a virgin sample, showing the original phase transition process marked by peak 1 in Figure 1h. Meanwhile, the MIT temperature of the VO<sub>2</sub> in area 2 marked by peak 2 would be tuned to lower temperature regime due to the increased Ne<sup>+</sup> concentration. Multienergy Ne<sup>+</sup> implantation was performed to clarify the relevance between the Ne<sup>+</sup> concentration and phase change temperature. After a double implantation process at the ion energy of 100 and 50 keV, two concentration peaks can be found in the Ne<sup>+</sup> distribution profile across the depth of the thin film (Figure 1f), which would create three layers with different Ne concentrations. Hence, three phase change processes can be observed in the Figure 1i. These results reveal that we can modify the MIT behavior of the VO<sub>2</sub> thin film in the out-of-plane dimension and create more than one phase profile in VO<sub>2</sub> thin films, which would provide a new route to design and fabricate the VO<sub>2</sub>-based devices, especially for the high-density memory applications.<sup>[24]</sup> Moreover, similar results are also obtained in He<sup>+</sup>-implanted samples (Figure S1, Supporting Information).

Due to the significantly different optical properties of insulating and metallic phases at THz frequency range, VO<sub>2</sub> thin films have attracted much attention to be applied as THz devices, such as optical switches and modulators.<sup>[25]</sup> Temperature-dependent THz transmission spectra for virgin and Ne<sup>+</sup>-implanted VO<sub>2</sub> thin films are shown in Figure 2a. The transmittance of virgin VO<sub>2</sub> thin film exhibits an abrupt change at the critical temperature of 341 K. This is in agreement with the result of the electrical transport measurements shown in Figure 1b. For Ne<sup>+</sup>-implanted samples, the MIT process (indicated by the area between two red-dashed lines in Figure 2a) shows a significant shift to a lower temperature. In Figure 2a, there are two issues worth to be discussed here. First, the broadening phase transition process provides a larger temperature window to change the THz transmittance from 100 to 0%, which

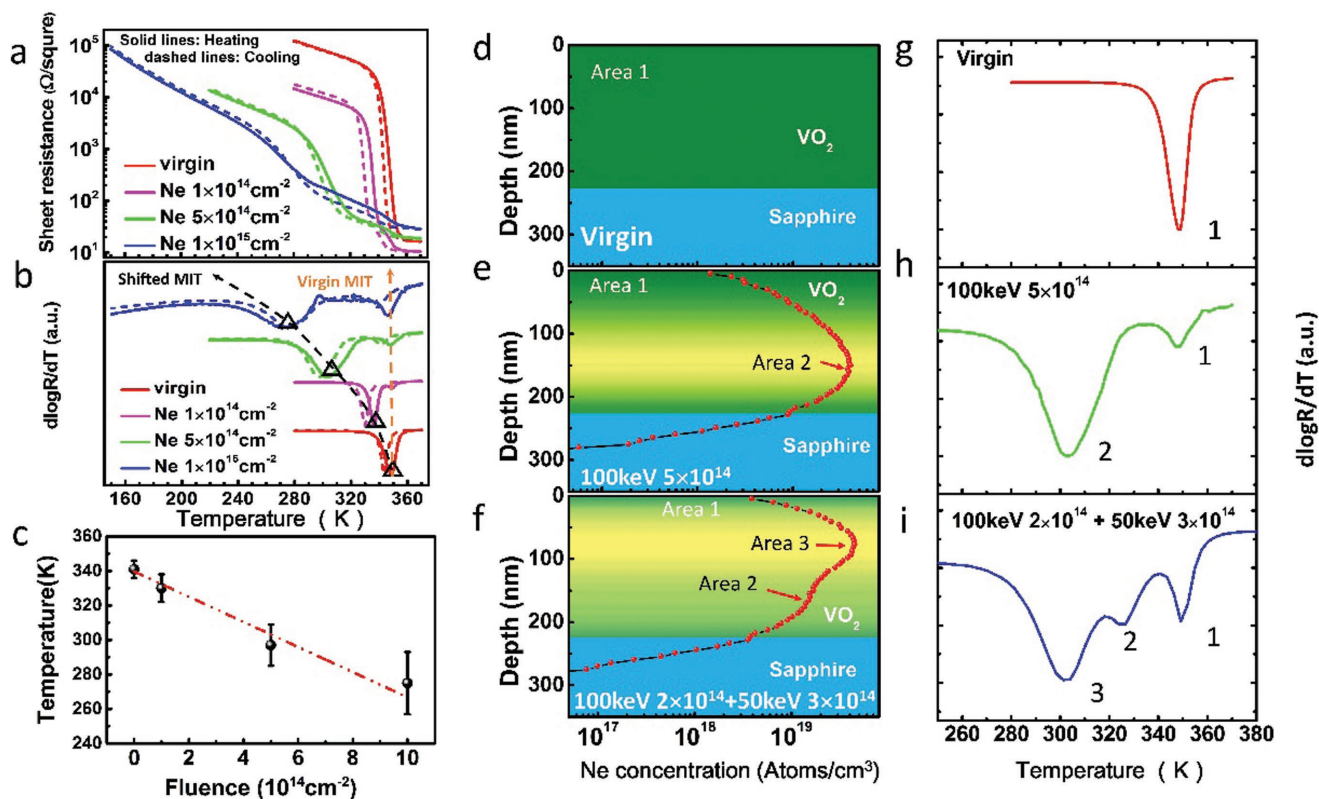


**Figure 1.** Electrical characterization of the MIT in VO<sub>2</sub> manipulated by Ne<sup>+</sup> implantation. a) The resistance as a function of temperature and b) their related differential curves of the virgin sample and Ne<sup>+</sup> implanted samples. The black triangle symbols in (b) indicate the significant reduction of the MIT temperature after Ne<sup>+</sup> implantation. The solid and the dashed lines refer to the heating process and the cooling process, respectively. c) The MIT temperature as the function of the Ne<sup>+</sup> fluence. d–f) The different depth profiles of the Ne<sup>+</sup> ions in VO<sub>2</sub> cross section created under two conditions: 1) 100 keV, 5 × 10<sup>14</sup> cm<sup>-2</sup> in (e) and 2) 100 keV, 2 × 10<sup>14</sup> cm<sup>-2</sup> plus 50 keV, 3 × 10<sup>14</sup> cm<sup>-2</sup> in (f) simulated by SRIM. g–i) The corresponding differential curves of the resistance as the function of temperature for the sample described in (d–f), respectively.

suggests a high potential for THz analog-like applications.<sup>[26]</sup> Second, VO<sub>2</sub> thin films implanted with different Ne<sup>+</sup> fluences exhibit different optical properties at the same temperature. For instance, at 320 K the virgin VO<sub>2</sub> thin film shows a high THz transmittance of around 80%, while the Ne<sup>+</sup>-implanted sample with the fluence of 5 × 10<sup>14</sup> cm<sup>-2</sup> shows a low THz transmittance of only 10%. This fancy phenomenon allows a new path to create the VO<sub>2</sub>-based THz metadevices by local noble gas implantation.

Raman spectra measurements were carried out to investigate the phase transition process of Ne<sup>+</sup>-implanted VO<sub>2</sub> thin films in more details. Figure 2b shows the Raman spectra of the virgin and the Ne<sup>+</sup>-implanted samples at room temperature. For the virgin sample, several peaks can be clearly observed (194, 225, 266, 308, 339, 390, 443, 489, and 614 cm<sup>-1</sup>), which corresponds to the Raman-active phonon modes in the insulating state.<sup>[27]</sup> None of the peaks associated with other forms of vanadium oxides have been detected, which suggests a highly pure VO<sub>2</sub> composition in our samples. With the increasing Ne<sup>+</sup> implantation fluence, all these Raman peaks become weak and finally disappear. For the Ne<sup>+</sup>-implanted samples, the weak Raman intensity in the implanted sample with the lower Ne<sup>+</sup> fluence (pink lines in Figure 2b) suggests a mixture of the insulator and metal phases at room temperature. With further increase of the

Ne<sup>+</sup> fluence, the metal phase becomes dominant in the film, which results in the absence of the Raman peaks. The temperature-dependent Raman spectra of the Ne<sup>+</sup>-implanted VO<sub>2</sub> thin film (Figure 2c–f) reveal that transition processes from the insulator phase to the metal phase occurred at reduced temperatures, which is in the agreement with the electrical and THz measurements.

X-ray diffraction measurements were performed to study the lattice modification of the Ne<sup>+</sup>-implanted samples. The epitaxy relationship between VO<sub>2</sub> thin film and Al<sub>2</sub>O<sub>3</sub>(0001) substrate can be determined as VO<sub>2</sub>[010]<sub>M1</sub>//Al<sub>2</sub>O<sub>3</sub>[0001] and VO<sub>2</sub>[102]<sub>M1</sub>//Al<sub>2</sub>O<sub>3</sub>[ $\bar{1}$  2  $\bar{1}$  0] (Figure S2a, Supporting Information).<sup>[28]</sup> Figure 3a shows the  $\omega$ -2 $\theta$  scans along the (020)<sub>M1</sub> reflection of the VO<sub>2</sub> thin films. The position of the VO<sub>2</sub>(020)<sub>M1</sub> peak was found at 2 $\theta$  = 39.9°. With the increasing Ne<sup>+</sup> fluence, the VO<sub>2</sub>(020)<sub>M1</sub> peak broadens, shifts toward smaller angles, and splits into several distinct peaks (green and blue lines in Figure 3a), revealing an expansion of the out-of-plane lattice constant induced by the noble gas implantation.<sup>[29]</sup> To get more specific information about the variations of VO<sub>2</sub> lattice parameters induced by Ne<sup>+</sup> implantation, reciprocal-space mappings (RSM) measurements were performed along both the out-of-plane and in-plane directions. High-resolution RSM images of VO<sub>2</sub>(020)<sub>M1</sub> and (23 $\bar{1}$ )<sub>M1</sub> peaks of virgin and Ne<sup>+</sup>-implanted samples are shown

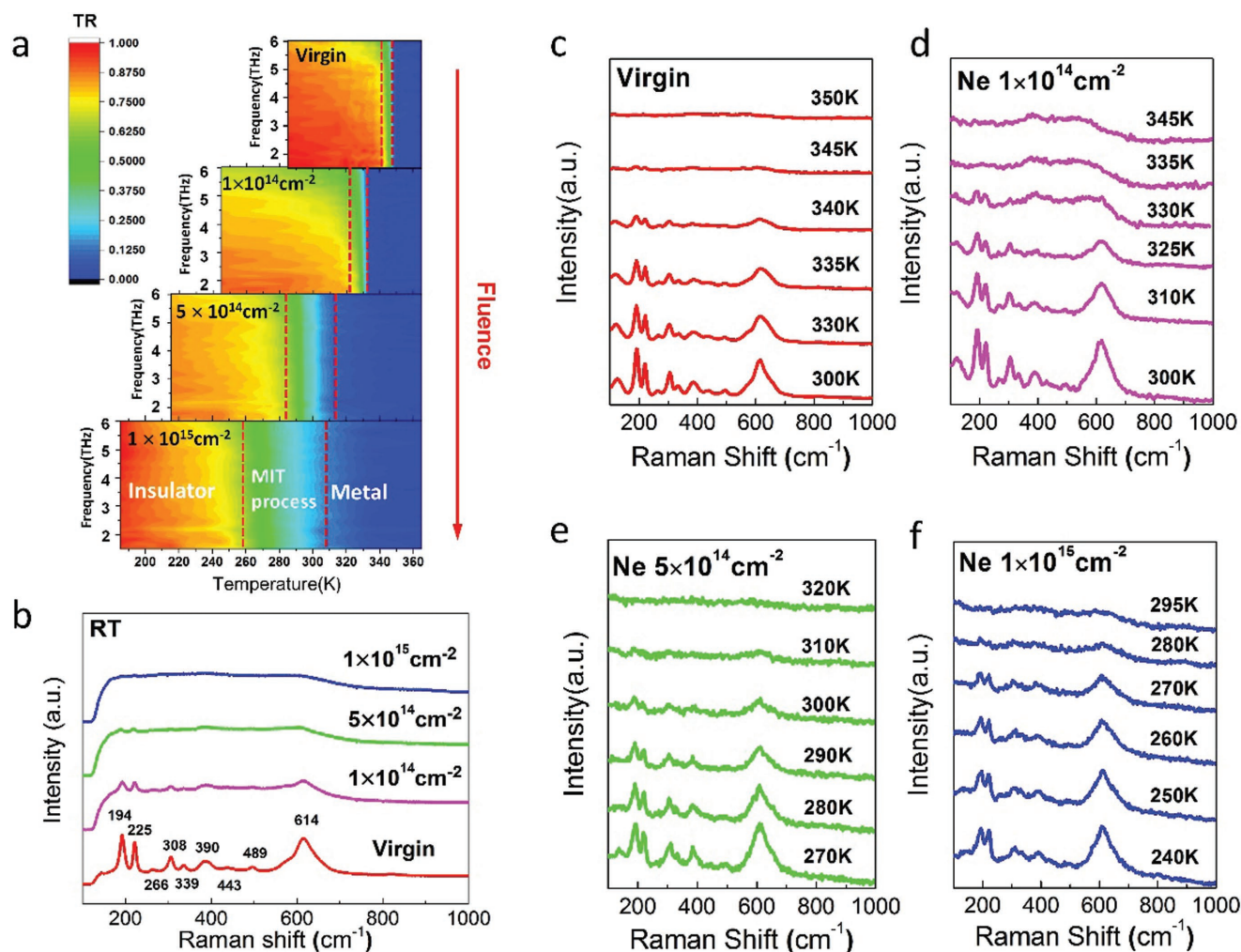


**Figure 2.** THz and Raman characterization of the MIT in VO<sub>2</sub> manipulated by Ne<sup>+</sup> implantation. a) Temperature dependence of the THz transmission spectra for virgin and Ne<sup>+</sup>-implanted VO<sub>2</sub> thin films. The areas between two red-dashed lines indicate the metal–insulator transition process, which reveals the decrease of phase transition temperature with increasing Ne<sup>+</sup> fluences (The two dashed lines refer to the transmission between 0.1 and 0.7.). The color scale refers to the transmittance information. b) Raman spectra for virgin and Ne<sup>+</sup>-implanted VO<sub>2</sub> samples at room temperature. Temperature-dependent Raman spectra for c) virgin sample and Ne<sup>+</sup> implanted sample with the fluence of d)  $1 \times 10^{14} \text{ cm}^{-2}$ , e)  $5 \times 10^{14} \text{ cm}^{-2}$ , and f)  $1 \times 10^{15} \text{ cm}^{-2}$ .

in Figure 3b. For higher fluences, the virgin peak and the peak induced by additional strain are clearly separated. As the Ne<sup>+</sup> fluence increases, these strain peaks move away from the virgin peak. With an Ne<sup>+</sup> fluence of  $5 \times 10^{14} \text{ cm}^{-2}$ , a clear strained layer has built up into the VO<sub>2</sub> thin film indicating that at least half of the VO<sub>2</sub> layer is affected. The appearance of a strained VO<sub>2</sub> layer peak beside the virgin one can be, in a very simple approximation (Figure S3, Supporting Information), interpreted that the virgin VO<sub>2</sub> layer splits into two parts, where one part did not change and corresponds almost to the virgin film and the other one exhibits a lattice expansion parallel to the surface normal resulting into a proportional volume increase. And indeed two transition temperatures can be observed in the implanted samples: The original one corresponding to the virgin film and a lowered one corresponding to the implanted film. Hence, the lattice values as a function of the fluence can be derived as shown in Figure 3c. For the virgin sample, the out-of-plane lattice spacing along  $d(010)_{M1}$  that corresponds to the *b*-axis is

about  $4.501 \text{ \AA}$  and the derived in-plane lattice value  $d(20\bar{1})_{M1}$  is about  $2.887 \text{ \AA}$ . Compared with the standard VO<sub>2</sub> lattice constant in ICDD(2008) 00-44-252 ( $b = d_{(010)M1} = 4.5263 \text{ \AA}$ ,  $d_{(-20\bar{1})M1} = 2.876 \text{ \AA}$ ),<sup>[30]</sup> the VO<sub>2</sub> thin virgin film grown on the Al<sub>2</sub>O<sub>3</sub>(0001) surface must suffer strain due to the lattice mismatch between VO<sub>2</sub> and the underlying substrate. As the Ne<sup>+</sup> fluence rises, the out-of-plane lattice increases, while the measured in-plane lattice value  $d(20\bar{1})_{M1}$  decreases, respectively, as shown in Figure 3c. We have derived an almost linear dependency of the lattice constants on the Ne<sup>+</sup> fluence of  $+0.01(0) \text{ \AA } 10^{-14} \text{ cm}^{-2}$  for the out-of-plane lattice and of  $-0.003(5) \text{ \AA } 10^{-14} \text{ cm}^{-2}$  for the in-plane values. In addition to the large-area reciprocal space mapping, pole figure measurements also suggests a good epitaxial quality and demonstrate a sixfold symmetry for the Ne<sup>+</sup>-implanted sample (Figure S2b, Supporting Information). As demonstrated in the ref. [19], noble gas ion implantation induces an uniaxial out-of-plane strain into an ultrathin film of 20 nm, and where the in-plane lattice constant is almost invariant since it

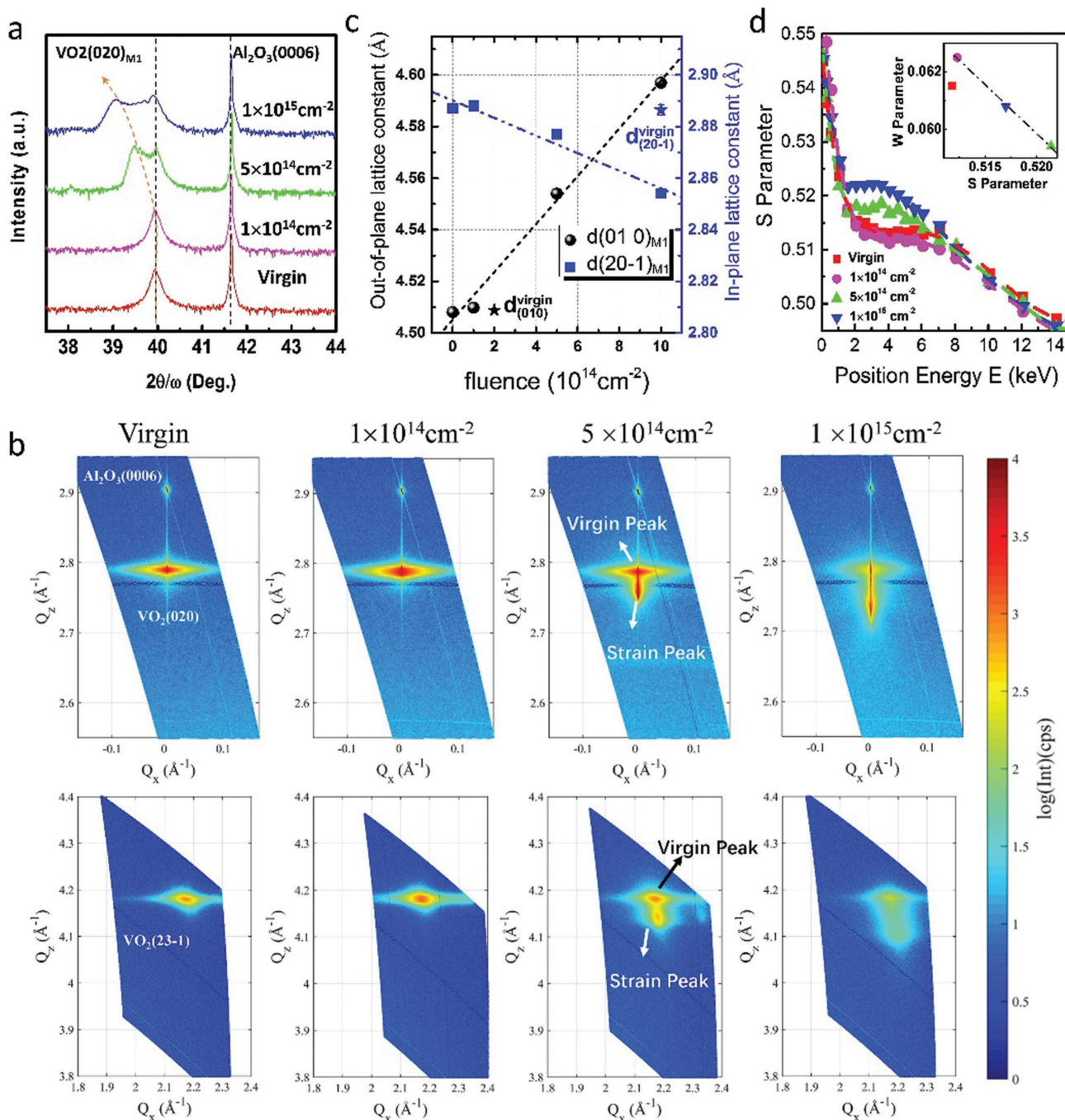


**Figure 3.** XRD and PAS analysis of the lattice modification in Ne<sup>+</sup>-implanted VO<sub>2</sub>. a) The  $\omega$ - $2\theta$  scan high-resolution XRD curves for virgin and Ne<sup>+</sup>-implanted VO<sub>2</sub> thin films at room temperature. b) The high-resolution reciprocal space mapping of virgin VO<sub>2</sub> and Ne<sup>+</sup>-implanted samples at the peak around VO<sub>2</sub> (020)<sub>M1</sub> and VO<sub>2</sub> (23 $\bar{1}$ )<sub>M1</sub> at room temperature. c) The out-of-plane (black dots) and in-plane (blue squares) lattice constant changes as a function of the Ne<sup>+</sup> fluence. The stars show the lattice constant of virgin out-of-plane (black) and in-plane (blue) lattice constant values derived over all samples with a corresponding error bar. d) S parameter as a function of incident position energy for virgin and Ne<sup>+</sup>-implanted VO<sub>2</sub> samples obtained by PAS. The inset shows W-S plot of PAS results measured from different VO<sub>2</sub> samples shown in (d).

is locked to that of the substrate.<sup>[19]</sup> But we have a much thicker film, of about 220 nm, the in-plane lattice is not anymore governed by the substrate. The Ne<sup>+</sup> implantation changes both the out-of-plane and in-plane lattice constant simultaneously according to the Poisson ratio of the VO<sub>2</sub>. The RSMs around the

asymmetrical (23 $\bar{1}$ )<sub>M1</sub> reflection nicely indicate that the implantation leads to an increasing stress that for larger fluences exceeded a certain threshold triggering a decrease of the in-plane lattice constant and, is therefore, accompanied by a reduction of the strain energy of the locally epitaxial bound VO<sub>2</sub> layer.

In order to characterize the defects induced by Ne<sup>+</sup> implantation in VO<sub>2</sub>, high-resolution cross-sectional transmission electron microscopy (XTEM) was performed (Figure S3b, Supporting Information). However, there are no observable contrast differences in the cross sections of the virgin and the implanted VO<sub>2</sub>. This indicates that the VO<sub>2</sub> thin films remain epitaxial quality after implantation at such low fluence, and XTEM seems not to be the suitable approach to obviously distinguish the defects generated in such relatively low fluence regime.<sup>[31]</sup> Alternatively, positron annihilation Doppler broadening spectroscopy measurement (PAS) is an excellent method to detect open volume defects ranging from a monovacancy to vacancy clusters consisting of about 25 vacancies.<sup>[32]</sup> In this measurement, *S* (shape) and *W* (wing) are the two major parameters of the Doppler broadened 511 keV line spectra. The measured *S* and *W* parameters give the information about the nature and concentration of open volume defects as well as the atomic environment of the annihilation (Note S1, Supporting Information). Figure 3d shows the *S*-parameters of the virgin and the Ne<sup>+</sup>-implanted samples as a function of the positron energy. The *S* parameter increases with the increasing Ne<sup>+</sup> implantation fluence, which indicates that more open volume defects are created by high Ne<sup>+</sup> fluence. In addition, as the position energy is positively correlated to the depth of the thin film, the profile of the *S* parameter confirms that there is an inhomogeneous open volume defects distribution resulting in a strain gradient along the out-of-plane direction. The inset of Figure 3d shows the *S*-*W* plot for different samples. A straight line is obtained from the *S*-*W* plot of the Ne<sup>+</sup>-implanted samples, while that of the virgin one deviates from the straight line. This indicates the different chemical environment of the open volume defect located in the virgin samples and in Ne<sup>+</sup>-implanted samples. The intrinsic defects in the virgin samples are generally empty vacancy clusters, while the extrinsic defects induced by Ne<sup>+</sup> implantation are open volume vacancies filled with Ne atoms.<sup>[33]</sup> Moreover, the out-of-plane strain profiles can be simulated by a recursive dynamical algorithm implemented in the commercial program “RC\_REF\_Sim\_Win” using high-resolution XRD data.<sup>[34]</sup> And the strain profiles induced by the open volume defects exhibit a Gaussian depth distribution as well (Figure S3a, Supporting Information).

Noble gas ion implantation with a relatively low fluence would create a certain amount of open volume defects in VO<sub>2</sub> thin film instead of deteriorating the crystalline structure of VO<sub>2</sub>.<sup>[19]</sup> The open volume defects induce the lattice variation and the corresponding strain in the thin film. To better understand the effect of lattice variations on the electronic structure of VO<sub>2</sub> thin film, a first-principle calculation based on DFT was performed. In the VO<sub>2</sub> thin film, the changes in the electronic band structure near the Fermi level plays a crucial role on the phase transition properties due to the strong hybridization between V3d and O2p electron bands.<sup>[35]</sup> As the noble gas does not introduce any electrical charge into VO<sub>2</sub> thin film, we have calculated the total density-of-states spectra (DOS) for the VO<sub>2</sub> samples with different out-of-plane lattice expansions or in-plane lattice contraction in M1 phase. As shown in Figure 4a,b, both the lattice expansion along the out-of-plane direction and the lattice contraction along the in-plane direction can reduce the electronic band gap above the Fermi level. Therefore, we calculated these two

situations separately since we want to figure out which situation shows a stronger effect. As shown in Figure 4a,b below, the lattice contraction along the in-plane direction is more effective. These lattice modifications decrease the band gap and reduce the energy barrier for phase transition in epitaxial VO<sub>2</sub> samples. Consequently, the phase transition of the Ne<sup>+</sup>-implanted VO<sub>2</sub> samples can be triggered at lower temperature. According to the crystal-field theory in VO<sub>2</sub>,<sup>[36]</sup> the energy levels near the Fermi level are mostly dominated by V<sub>3d</sub> orbitals and the V<sub>3d</sub> energy levels are split into a low-energy *t*<sub>2g</sub> state and a high-energy *e*<sub>σg</sub> state. The *t*<sub>2g</sub> level is further split into a single *a*<sub>1g</sub> orbital and a doubly degenerate *e*<sub>πg</sub> orbital. Among them, the *a*<sub>1g</sub> band, also termed as *d*<sub>//</sub>, is nonbonding with the O<sub>2p</sub> levels and parallel to the direction of V-V bond (the direction along (201)<sub>M1</sub>). Meanwhile, the *e*<sub>σg</sub> and *e*<sub>πg</sub> levels will form the low-energy bonding states (*σ* and *π* bands) and the high-energy nonbonding states (*σ*<sup>\*</sup> and *π*<sup>\*</sup> bands). In the M1 phase, the *d*<sub>//</sub> orbital is split into a bonding state and an antibonding state (*d*<sub>//</sub> and *d*<sub>//</sub><sup>\*</sup>) due to the distortion of V-V chains, as shown in Figure 4c. According to the RSM results, the expansion of out-of-plane lattice spacing and contraction of in-plane lattice spacing can both depress the p-d overlap and the related hybridization. As demonstrated in Figure 4d, the *d*<sub>//</sub><sup>\*</sup> orbital would shift upward, while the *d*<sub>//</sub> and *π*<sup>\*</sup> band would shift downward after Ne<sup>+</sup> implantation. Consequently, the band gap becomes narrower, and the phase change temperature is lowered. There is an agreement between the first-principle calculation and the experimental results.

Furthermore, in order to explore the local manipulation of the MIT behavior of VO<sub>2</sub> thin films and the patterning capability of this method for device applications, area-selective Ne<sup>+</sup> implantation with the fluence of 5 × 10<sup>14</sup> cm<sup>-2</sup> (100 keV) were carried out on a VO<sub>2</sub> thin film by photolithography, as shown in Figure 5a. The pattern is designed as a double “C” structure, which is a typical structure applied in metamaterials.<sup>[37]</sup> The Raman spectra measured from the implanted area and virgin area in one chip at room temperature were shown in Figure 5b. It is found that the implanted area has a typical spectrum of the metallic phase, in contrast, the spectra of the unimplanted area shows the peaks of insulating phase. As shown in Figure 5c, the optical microscope and Raman spectroscopy images produced using the integrated intensity of the photon mode at 614 cm<sup>-1</sup> of this sample. At a temperature of 250 K, the implanted and virgin area are both in the insulating state, and the photon mode at 614 cm<sup>-1</sup> is intensive (black). As the temperature increases, the phase change process occurs in the implanted area in advance. A clear optical microscope and Raman image of the structure can be observed at room temperature. As the temperature rises to 370 K, the whole sample shows the metallic behavior (red). The entire cooling process recorded by the optical microscope is shown in the Video S1 (Supporting Information). This significant change indicates the potential application of the above method to fabricate temperature-controlled VO<sub>2</sub> THz metasurface or smart windows. As mentioned earlier, He implantation has the similar effect on modification of the MIT transition in VO<sub>2</sub> thin film. Thanks to the extremely high lateral and vertical resolution of sub-5 nm, the technique of He ion microscope can directly write the nanoscale pattern on VO<sub>2</sub> thin film and fabricate the VO<sub>2</sub>-based nanodevices without any deposition and etching processes.<sup>[38]</sup>

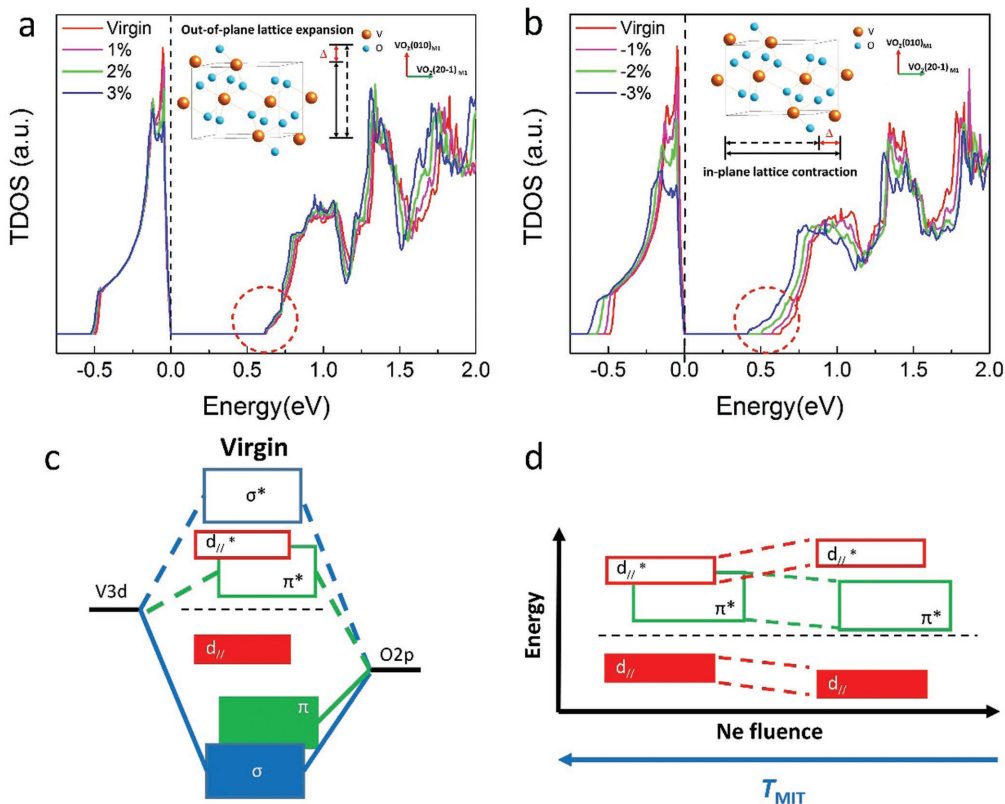


**Figure 4.** First principle calculation of MIT manipulation by lattice engineering. The calculated total DOS for the VO<sub>2</sub> film with a) different out-of-plane lattice spacing along (020)<sub>M1</sub> expansions and b) different in-plane lattice spacing along (20 $\bar{1}$ )<sub>M1</sub> contractions (Fermi level set to zero). The inset shows the scheme for Ne<sup>+</sup> implantation induced out-of-plane lattice expansion and in-plane lattice contraction in M1 phase of VO<sub>2</sub> thin films grown on sapphire (0001). The dashed circles indicate that the conductive band would shift toward the Fermi level. c) The electronic band scheme for VO<sub>2</sub> in insulator state and its changes after Ne<sup>+</sup> implantation d).

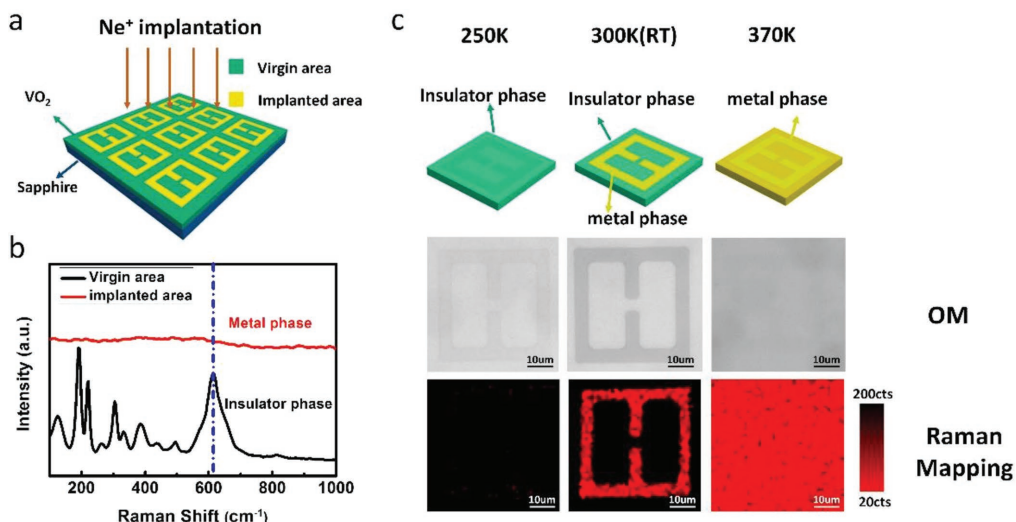


**Figure 5.** Local manipulation of MIT in VO<sub>2</sub> with patterned Ne<sup>+</sup> implantation. a) The schematic representation for patterned implantation into VO<sub>2</sub> thin films by photolithography. The virgin area is shadowed by the mask and only the yellow area is exposed to the Ne<sup>+</sup> implantation. b) Room temperature Raman spectra for the virgin and patterned implanted area with a fluence of  $5 \times 10^{14} \text{ cm}^{-2}$  in one chip. c) The images of the optical microscope and Raman mapping for the peak around  $614 \text{ cm}^{-1}$  at 250, 300, and 370 K.

### 3. Conclusion

In conclusion, we have demonstrated that noble gas ion implantation is an effective way to symmetrically modify the metal–insulator transition temperature in VO<sub>2</sub> thin films grown on Al<sub>2</sub>O<sub>3</sub>(0001). The noble gas ion implantation may create the open volume defects which can generate a lattice strain in VO<sub>2</sub> crystal lattices. The changes of lattice structure induce the modification of the electronic structure and result in the reduction of the MIT temperature in VO<sub>2</sub> thin films. Based on these findings, patterned insulating and metallic areas on a VO<sub>2</sub> surface at room temperature were fabricated by Ne<sup>+</sup> implantation together with lithography, and a multilevel MIT transition was realized after locally modifying the VO<sub>2</sub> cross section as well. The demonstrated method to locally tailor the MIT behavior both on the surface and in the cross section of the thin film will be a powerful tool to develop novel electrical/optical structures and devices by using strongly correlated materials, e.g., metamaterials,<sup>[39]</sup> single atom transistor,<sup>[40]</sup> high-density memory device,<sup>[5,24]</sup> and so on.

### 4. Experimental Section

**Sample Preparation:** The VO<sub>2</sub> samples with the thickness of around 220 nm were deposited on sapphire (0001) substrates by PLD workstation from Surface systems + Technology GmbH. The deposition temperature of 903 K, the KrF laser energy of 1.6 J cm<sup>-2</sup>, and oxygen partial pressure of 1.3 × 10<sup>-2</sup> mbar were applied. Then, these samples were implanted by 100 keV Ne<sup>+</sup> ions with the fluence of 1 × 10<sup>14</sup> cm<sup>-2</sup>, 5 × 10<sup>14</sup> cm<sup>-2</sup>, and 1 × 10<sup>15</sup> cm<sup>-2</sup>, respectively. Alternatively, a VO<sub>2</sub> sample was implanted with the fluence of 2 × 10<sup>14</sup> cm<sup>-2</sup> at 100 keV and 3 × 10<sup>14</sup> cm<sup>-2</sup> at 50 keV.

**Electrical Characterization:** The electrical transport measurements of VO<sub>2</sub> samples were carried out by Lakeshore Hall Effect Measurements System (9700A). The four electrical connections were made by Ag wires connected to the four corners of squared samples by silver paste according to the Van der Pauw method. The measurement temperature was taken from 280 to 370 K by the increment of 0.5 K, and both heating and cooling process were performed.

**X-ray Diffraction Characterization:** XRD was performed by an Empyrean Panalytical diffractometer with a Cu-target source. The setup was equipped with a Göbel mirror and an asymmetric monochromator to enhance the brilliance and monochromaticity. The reciprocal space maps were recorded using an Area-(Pixel-)Detector (516 × 516 pixels with 55 μm pixel size) that was able to cover more than 6° in 2θ, for the 2θ/ω symmetrical line scans, a 0.2 mm slit in front of a point detector was used to obtain an optimal signal to noise ratio for the diffracted signal.

**Raman Spectroscopy:** The temperature dependence of Raman spectra was performed by HORIBA XploRA INV Raman system. The excitation wavelength used was 532 nm and the laser power was 100 mW. A 50 × objective lens was used with a laser point size of about 0.5 μm. Raman mapping measurements were carried out by the SWIFT ultrafast Raman imaging mode with the spatial resolution of 1 μm. The virgin and Ne<sup>+</sup> implanted samples were heated from 200 to 370 K by the Linkam THMS600 Thermal Stage system.

**Theoretical Calculation:** DFT calculations in this paper were carried out using the Vienna Ab initio Simulation Package with the Perdew–Burke–Ernzerhof exchange–correlation functional and generalized gradient approximation (GGA). The geometric structure optimization was performed using the conjugated-gradient minimization scheme until the maximum residual force on each atom was less than 0.01 eV Å<sup>-1</sup>. A plane-wave cutoff of 550 eV for vanadium was used in

the calculations, and the energies were converged to 10<sup>-6</sup> eV per atom. A 1 × 2 × 2 supercell was used for VO<sub>2</sub> M1 phase and the reciprocal space of M1 phase was sampled with a 9 × 9 × 9 Monkhorst–Pack grid. The GGA+U (with an effective U = 2.7 eV) was used for the strongly correlated d electrons of vanadium atoms.

### Supporting Information

Supporting Information is available from the Wiley Online Library or from the author.

### Acknowledgements

This work was supported by the National Science Fund of China (Nos. 11622545 and U1732268), Frontier Science Key Program of CAS (No. QYZDY-SSW-JSC032), One Hundred Talent Program of CAS, International Collaboration Project of Shanghai (No. 16520721100). Support by the Ion Beam Center at Helmholtz-Zentrum Dresden-Rossendorf is gratefully acknowledged.

### Conflict of Interest

The authors declare no conflict of interest.

### Keywords

lattice engineering, metal–insulator transition, open volume defect, vanadium dioxide

Received: October 2, 2017

Revised: December 4, 2017

Published online:

- [1] a) M. Imada, A. Fujimori, Y. Tokura, *Rev. Mod. Phys.* **1998**, *70*, 1039; b) M. M. Qazilbash, M. Brehm, B.-G. Chae, P.-C. Ho, G. O. Andreev, B.-J. Kim, S. J. Yun, A. Balatsky, M. Maple, F. Keilmann, *Science* **2007**, *318*, 1750; c) Z. Yang, C. Ko, S. Ramanathan, *Annu. Rev. Mater. Res.* **2011**, *41*, 337.
- [2] a) Z. Tao, T.-R. T. Han, S. D. Mahanti, P. M. Duxbury, F. Yuan, C.-Y. Ruan, K. Wang, J. Wu, *Phys. Rev. Lett.* **2012**, *109*, 166406; b) T. Yao, X. Zhang, Z. Sun, S. Liu, Y. Huang, Y. Xie, C. Wu, X. Yuan, W. Zhang, Z. Wu, *Phys. Rev. Lett.* **2010**, *105*, 226405.
- [3] J. Zhou, Y. Gao, Z. Zhang, H. Luo, C. Cao, Z. Chen, L. Dai, X. Liu, *Sci. Rep.* **2013**, *3*, 3029.
- [4] T. Yajima, T. Nishimura, A. Toriumi, *Nat. Commun.* **2015**, *6*, 10104.
- [5] Y. Zhou, X. Chen, C. Ko, Z. Yang, C. Mouli, S. Ramanathan, *IEEE Electron Device Lett.* **2013**, *34*, 220.
- [6] a) R. M. Briggs, I. M. Pryce, H. A. Atwater, *Opt. Express* **2010**, *18*, 11192; b) L. Pellegrino, N. Manca, T. Kanki, H. Tanaka, M. Biasotti, E. Bellingeri, A. S. Siri, D. Marré, *Adv. Mater.* **2012**, *24*, 2929.
- [7] a) J. M. Baik, M. H. Kim, C. Larson, C. T. Yavuz, G. D. Stucky, A. M. Wodtke, M. Moskovits, *Nano Lett.* **2009**, *9*, 3980; b) E. Strelcov, Y. Lilach, A. Kolmakov, *Nano Lett.* **2009**, *9*, 2322.
- [8] a) P. Jin, S. Nakao, S. Tanemura, *Thin Solid Films* **1998**, *324*, 151; b) K. Shibuya, M. Kawasaki, Y. Tokura, *Appl. Phys. Lett.* **2010**, *96*, 2102; c) J. G. Ramirez, T. Saerbeck, S. Wang, J. Trastoy, M. Malnou, J. Lesueur, J.-P. Crocombette, J. E. Villegas, I. K. Schuller, *Phys. Rev.*

- B **2015**, 91, 205123; d) H. Hofsäss, P. Ehrhardt, H.-G. Gehrke, M. Brötzmann, U. Vetter, K. Zhang, J. Krauser, C. Trautmann, C. Ko, S. Ramanathan, *AIP Adv.* **2011**, 1, 032168.
- [9] a) Y. Muraoka, Z. Hiroi, *Appl. Phys. Lett.* **2002**, 80, 583; b) L. Fan, S. Chen, Z. Luo, Q. Liu, Y. Wu, L. Song, D. Ji, P. Wang, W. Chu, C. Gao, *Nano Lett.* **2014**, 14, 4036; c) M. Liu, M. Wagner, E. Abreu, S. Kittiwatanakul, A. McLeod, Z. Fei, M. Goldflam, S. Dai, M. Fogler, J. Lu, *Phys. Rev. Lett.* **2013**, 111, 096602.
- [10] a) C. Wu, F. Feng, J. Feng, J. Dai, L. Peng, J. Zhao, J. Yang, C. Si, Z. Wu, Y. Xie, *J. Am. Chem. Soc.* **2011**, 133, 13798; b) H. Yoon, M. Choi, T.-W. Lim, H. Kwon, K. Ihm, J. K. Kim, S.-Y. Choi, J. Son, *Nat. Mater.* **2016**, 15, 1113.
- [11] a) S. Chen, L. Fan, G. Liao, Y. Chen, W. Chu, L. Song, J. Jiang, C. Zou, *Adv. Funct. Mater.* **2016**, 26, 3532; b) J. Jeong, N. Aetukuri, T. Graf, T. D. Schladt, M. G. Samant, S. S. Parkin, *Science* **2013**, 339, 1402.
- [12] a) D. Hilton, R. Prasankumar, S. Fourmaux, A. Cavalleri, D. Brassard, M. El Khakani, J. Kieffer, A. Taylor, R. Averitt, *Phys. Rev. Lett.* **2007**, 99, 226401; b) H. T. Zhang, L. Guo, G. Stone, L. Zhang, Y. X. Zheng, E. Freeman, D. W. Keefer, S. Chaudhuri, H. Paik, J. A. Moyer, *Adv. Funct. Mater.* **2016**, 26, 6612; c) S. Lysenko, V. Vikhnin, A. Rúa, F. Fernández, H. Liu, *Phys. Rev. B* **2010**, 82, 205425.
- [13] T. Driscoll, H.-T. Kim, B.-G. Chae, B.-J. Kim, Y.-W. Lee, N. M. Jokerst, S. Palit, D. R. Smith, M. Di Ventra, D. N. Basov, *Science* **2009**, 325, 1518.
- [14] a) H. L. Tuller, S. R. Bishop, *Annu. Rev. Mater. Res.* **2011**, 41, 369; b) S. V. Kalinin, N. A. Spaldin, *Science* **2013**, 341, 858.
- [15] a) K. Ahn, T. Lookman, A. Bishop, *Nature* **2004**, 428, 401; b) Y. Zhang, J. Lian, C. M. Wang, W. Jiang, R. C. Ewing, W. J. Weber, *Phys. Rev. B* **2005**, 72, 094112.
- [16] Z. Li, F. Chen, *Appl. Phys. Rev.* **2017**, 4, 011103.
- [17] S. Mathew, A. Annadi, T. K. Chan, T. C. Asmara, D. Zhan, X. R. Wang, S. Azimi, Z. Shen, A. Rusydi, M. B. Breese, *ACS Nano* **2013**, 7, 10572.
- [18] S. Saremi, R. Xu, L. R. Dedon, J. A. Mundy, S. L. Hsu, Z. Chen, A. R. Damodaran, S. P. Chapman, J. T. Evans, L. W. Martin, *Adv. Mater.* **2016**, 28, 10750.
- [19] a) H. Guo, S. Dong, P. D. Rack, J. D. Budai, C. Beekman, Z. Gai, W. Siemons, C. Gonzalez, R. Timilsina, A. T. Wong, *Phys. Rev. Lett.* **2015**, 114, 256801; b) A. Herklotz, S. F. Rus, T. Z. Ward, *Nano Lett.* **2016**, 16, 1782.
- [20] A. Ramadan, R. Gould, A. Ashour, *Thin Solid Films* **1994**, 239, 272.
- [21] F. C. Case, *J. Vac. Sci. Technol., A* **1984**, 2, 1509.
- [22] T. Yajima, T. Nishimura, A. Toriumi, *Small* **2017**, 13, 12.
- [23] J. F. Ziegler, M. D. Ziegler, J. P. Biersack, *Nucl. Instrum. Methods Phys. Res., Sect. B* **2010**, 268, 1818.
- [24] M. J. Lee, Y. Park, D. S. Suh, E. H. Lee, S. Seo, D. C. Kim, R. Jung, B. S. Kang, S. E. Ahn, C. B. Lee, *Adv. Mater.* **2007**, 19, 3919.
- [25] a) P. Markov, R. E. Marvel, H. J. Conley, K. J. Miller, R. F. Haglund Jr., S. M. Weiss, *ACS Photonics* **2015**, 2, 1175; b) M. Liu, H. Y. Hwang, H. Tao, A. C. Strikwerda, K. Fan, G. R. Keiser, A. J. Sternbach, K. G. West, S. Kittiwatanakul, J. Lu, *Nature* **2012**, 487, 345; c) H.-T. Chen, W. J. Padilla, J. M. Zide, A. C. Gossard, A. J. Taylor, R. D. Averitt, *Nature* **2006**, 444, 597.
- [26] G. Karaoglan-Bebek, M. Hoque, M. Holtz, Z. Fan, A. Bernussi, *Appl. Phys. Lett.* **2014**, 105, 201902.
- [27] a) H.-T. Kim, B.-G. Chae, D.-H. Youn, G. Kim, K.-Y. Kang, S.-J. Lee, K. Kim, Y.-S. Lim, *Appl. Phys. Lett.* **2005**, 86, 242101; b) J. Parker, *Phys. Rev. B* **1990**, 42, 3164.
- [28] Y. Ji, Y. Zhang, M. Gao, Z. Yuan, Y. Xia, C. Jin, B. Tao, C. Chen, Q. Jia, Y. Lin, *Sci. Rep.* **2014**, 4, 4854.
- [29] a) M. Servidori, *Nucl. Instrum. Methods Phys. Res., Sect. B* **1987**, 19, 443; b) H. Wen, L. Guo, E. Barnes, J. H. Lee, D. A. Walko, R. D. Schaller, J. A. Moyer, R. Misra, Y. Li, E. M. Dufresne, *Phys. Rev. B* **2013**, 88, 165424; c) H. Wen, P. Chen, M. P. Cosgriff, D. A. Walko, J. H. Lee, C. Adamo, R. D. Schaller, J. F. Ihlefeld, E. M. Dufresne, D. G. Schlom, *Phys. Rev. Lett.* **2013**, 110, 037601.
- [30] K. Rogers, *Powder Diffr.* **1993**, 8, 240.
- [31] Y. Wang, Y. Liu, E. Wendler, R. Hübner, W. Anwand, G. Wang, X. Chen, W. Tong, Z. Yang, F. Munnik, *Phys. Rev. B* **2015**, 92, 174409.
- [32] R. W. Siegel, *Annu. Rev. Mater. Sci.* **1980**, 10, 393.
- [33] X. Ou, R. Kogler, H. B. Zhou, W. Anwand, J. Grenzer, R. Hubner, M. Voelskow, M. Butterling, S. Q. Zhou, W. Skorupa, *Phys. Rev. B* **2012**, 86, 224103.
- [34] P. Zaumseil, *Phys. Status Solidi A* **1998**, 165, 195.
- [35] B. Qu, H. He, B. Pan, *J. Appl. Phys.* **2011**, 110, 113517.
- [36] a) J. B. Goodenough, *J. Solid State Chem.* **1971**, 3, 490; b) J. B. Goodenough, *Phys. Rev.* **1960**, 117, 1442; c) N. B. Aetukuri, A. X. Gray, M. Drouard, M. Cossale, L. Gao, A. H. Reid, R. Kukreja, H. Ohldag, C. A. Jenkins, E. Arenholz, *Nat. Phys.* **2013**, 9, 661.
- [37] D. R. Smith, J. B. Pendry, M. C. Wiltshire, *Science* **2004**, 305, 788.
- [38] J. Notte, J. Huang, *Helium Ion Microscopy*, Springer, **2016**, p. 3.
- [39] L. Liu, L. Kang, T. S. Mayer, D. H. Werner, *Nat. Commun.* **2016**, 7, 13236.
- [40] M. Fuechsle, J. A. Miwa, S. Mahapatra, H. Ryu, S. Lee, O. Warschkow, L. C. Hollenberg, G. Klimeck, M. Y. Simmons, *Nat. Nanotechnol.* **2012**, 7, 242.